SCIENTIFIC REPORTS
nature research

OPEN

Emerging WS_2/montmorillonite composite nanosheets as an efficient hydrophilic photocatalyst for aqueous phase reactions

Kang Peng[1], Hongjie Wang[1*], Xiaoyu Li[2], Jianwei Wang[1], Zhixin Cai[1], Lei Su[1] & Xingyu Fan[1]

Tungsten disulfide (WS_2) as one of transition metal dichalcogenides exhibits excellent catalytic activity. However, its catalytic performances in aqueous phase reactions are limited by its hydrophobicity. Here, the natural hydrophilic two-dimensional clay was used to enhance the dispersibility of WS_2 in aqueous phase. WS_2/montmorillonite (WS_2/MMT) composite nanosheets were prepared via hydrothermal synthesis of WS_2 on the surface of montmorillonite from WCl_6 and CH_3CSNH_2. The microstructure and morphology show that WS_2 nanosheets are assembled parallelly on the montmorillonite with the interface interaction. Through the support of montmorillonite, WS_2/MMT possesses higher photocatalytic ability for aqueous phase reactions than WS_2, which could be due to the synergistic effect of higher adsorption property, higher hydrophilicity, dispersibility and more catalytic reaction site. The strategy could provide new ideas for obtaining novel hydrophilic photocatalyst with excellent performance.

Since the discovery of graphene, two dimensional (2D) materials have pioneered a new field for nanomaterials. Due to their specific structure and unconventional physicochemical property, 2D nanomaterials have received world-wide of attention for energy storage and conversion[1], electronics[2] and catalysis[3,4]. In addition to graphene, many novel 2D nanomaterials have been found and researched heavily in recent years[5], such as transition metal dichalcogenide (TMD)[6,7], layered double hydroxides (LDHs)[8] and graphene analogues[9,10]. Various 2D composite nanosheets were designed and fabricated via multifarious methods[11], which exhibit exceptional properties and play important roles in many high-tech fields.

Recently, TMD has attracted a lot of attention due to peculiar electrical and optical characteristics and intrinsic semiconducting properties[12]. Interestingly, their electronic band gap transform into direct band gap from indirect band gap, with thickness decreasing to monolayer or few layers from bulk[13]. Tungsten disulfide (WS_2) with sandwich structure is a kind of TMD composed of multilayered nanosheets[14,15]. WS_2 sheets possess high absorption for the visible light and excellent photocatalytic activity[16], which could be used in hydrogen evolution[17], degradation of dyes[18] and reduction of nitrophenol[19]. The photocatalytic ability of WS_2 nanosheets might mainly originate from unsaturated atoms on the surfaces and edges[20,21]. It is reported that the theoretical conduction band and valance band of WS_2 are −0.06 and 2.27 eV[22], and WS_2 has photocatalytic hydrogen production performance[21]. Conventional methods to obtain few-layered WS_2 sheets include mechanical exfoliation and chemical vapor deposition. Hydrothermal synthesis using precursor of sodium molybdate could obtain fullerene-like WS_2 nanoparticles, 1D nanotubes and rods, but 2D nanosheets is hard to get in this way. Jieun Yang and co-workers[23] first report the synthesis of WS_2/graphene nanosheets by hydrothermal method from tungsten chloride at 265 °C. The WS_2 nanosheets easily aggregate to reduce catalytic activity, and assembling them on the support materials is one of effective solutions. WS_2 and most WS_2 composites are hydrophobicity and poor dispersibility in aqueous phase. Therefore, design of hydrophilic WS_2 composites is significant for their catalytic ability in aqueous phase.

Montmorillonite (MMT) is one of natural sheet-like clay mineral with excellent hydrophobicity. Its layer structure consists of a central Al-O octahedral sheet and two Si-O tetrahedral sheets, and the unit layer stacks with cation in the interlayer. MMT possesses large special surface area, excellent adsorptive capacity and hydrophobicity, which make it a promising material for pollutants adsorption, catalyst supports[24–27], wastewater treatment[28,29],

[1]State Key Laboratory for Mechanical Behavior of Materials, Xi'an Jiaotong University, Xi'an, 710049, China. [2]School of Materials Science and Engineering, Chang'an University, Xi'an, 710064, China. *email: hjwang@xjtu.edu.cn

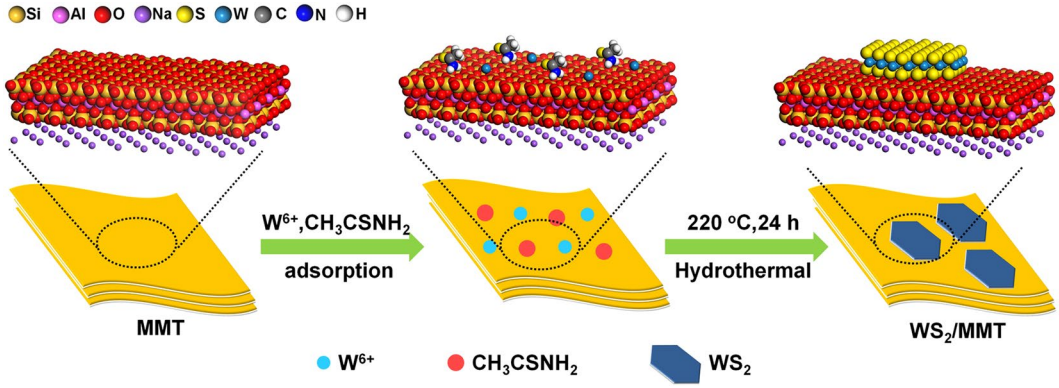

Figure 1. Schematic representation for the hydrothermal preparation of WS_2/MMT.

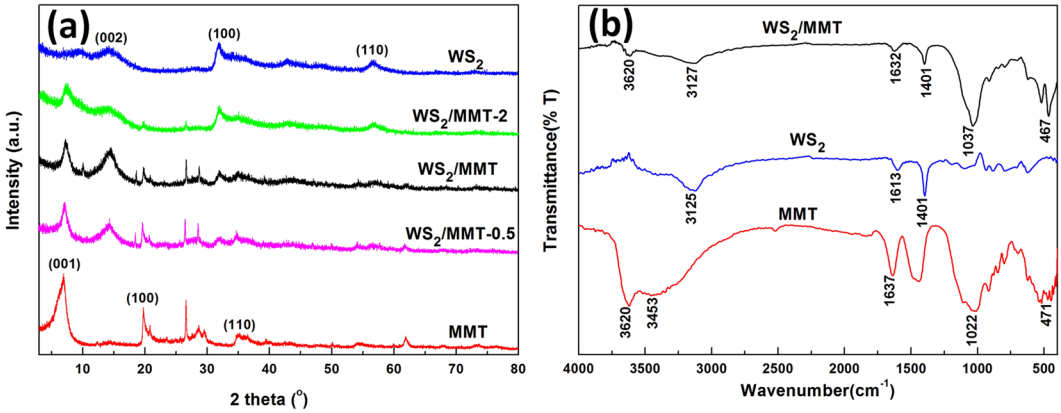

Figure 2. Phase structure and vibrational bands of the samples. (**a**) XRD patterns of MMT, WS_2, WS_2/MMT, WS_2/MMT-0.5 and WS_2/MMT-2. (**b**) FTIR spectra of MMT, WS_2 and WS_2/MMT.

energy storage matrix[30,31] and drug delivery systems[32]. Based on the special structure and property of MMT, hydrophilic composite nanosheets might be constructed through MMT supporting WS_2 nanosheets, which could be used as an efficient photocatalyst for aqueous phase reactions. Hazardous wastewaters with organic dye are greatly harmful to the environment[33–37]. Photocatalysis technology is a potential approach to treat these waste waters[38], and design of the efficient photocatalyst is one of the key procedures[39,40].

Herein, we first designed and prepared the WS_2/montmorillonite (WS_2/MMT) composite nanosheets as a hydrophilic photocatalyst for aqueous phase reactions. WS_2/MMT was successfully fabricated through facile *in-situ* hydrothermal synthesis of WS_2 on MMT. The microstructure and morphology were characterized, and the photocatalytic ability for aqueous phase reactions was evaluated by degradation of organic dye. The effect of MMT on catalytic ability was studied, and the possible catalysis mechanism for photocatalytic degradation of RhB were explored and illustrated in detail.

Results

As schematically depicted in Fig. 1, the WS_2/montmorillonite (WS_2/MMT) composite nanosheets were hydrothermally synthesized with tungsten chloride and thioacetamide at 220 °C for 24 h. Firstly, the montmorillonite (MMT) was added in water solution of WCl_6 and CH_3CSNH_2. The surface of MMT is negatively charged for the Si^{4+} lattice replaced by Al^{3+}. Conventional tungstate precursors such as Na_2WO_4 and $(NH_4)_{10}W_{12}O_{41}$ are unable to adsorb on of MMT. Therefore, WCl_6 was employed as a precursor of tungsten, and W^{6+} was adsorbed on MMT by electrostatic interaction. In hydrothermal conditions, the thioacetamide was pyrolyzed and released H_2S, and WCl_6 was reduced to form WS_2 by sulfurization. Finally, the WS_2 nanosheets were nucleated and grown, and the as-prepared WS_2 was assembled on MMT to prepare WS_2/MMT nanosheets.

The crystallographic structure was inspected by XRD measurements, and the patterns of MMT, WS_2, WS_2/MMT, WS_2/MMT-0.5 and WS_2/MMT-2 are presented in Fig. 2a. In the pattern of MMT, the reflection at 7.2° (2θ) is attributed to the (001) reflection of Na-montmorillonite, indicating that the d_{001} basal spacing is 1.22 nm. The diffraction peaks at 19.7° and 34.7° (2θ) are corresponding to (100) and (110) planes of MMT. The diffraction peaks in the pattern of hydrothermally synthesized WS_2 can be attributed to 2H-WS_2 phase (JCPDS#08-0237). The reflection at 14.2° due to the (002) diffraction shows the distance of lattice plane along (002) is 0.62 nm for WS_2 multilayer. The reflections assigned to (100) and (110) planes of WS_2 are found at 32.7° and 58.4°, respectively. The main reflections of MMT and WS_2 were observed in XRD pattern of WS_2/MMT. Compared with WS_2/

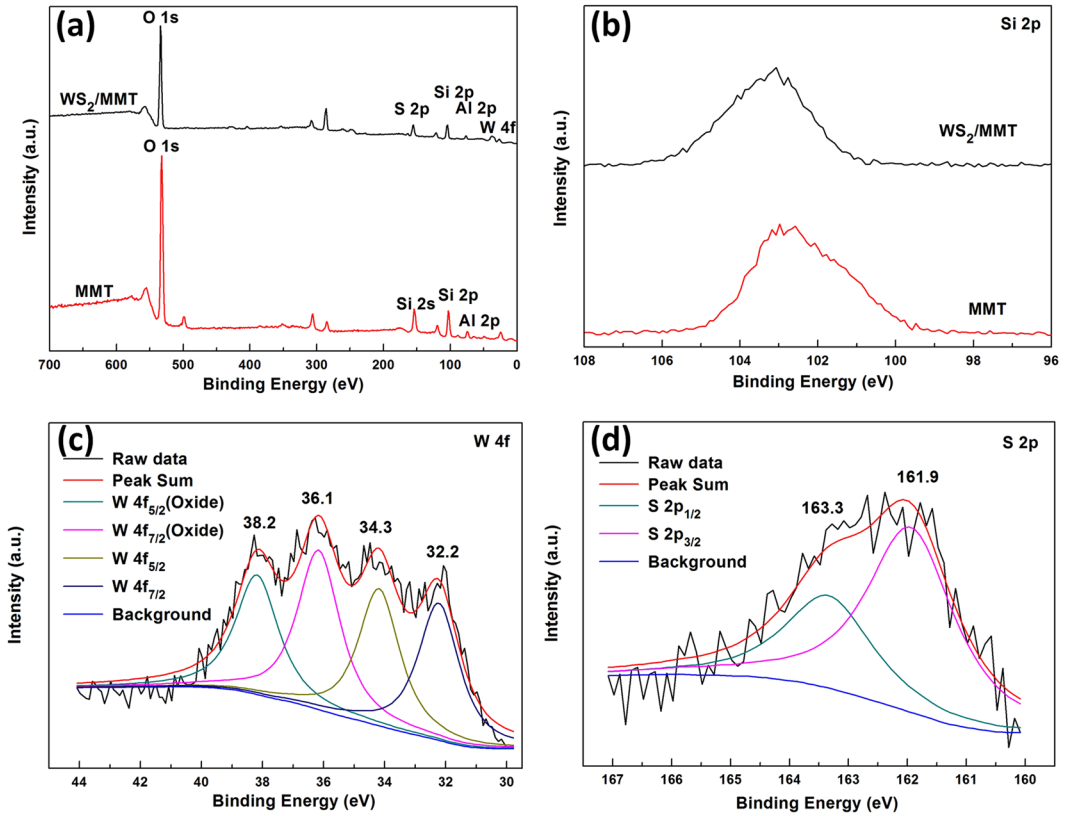

Figure 3. Interface characteristics and chemical status. (**a**) XPS survey spectra and (**b**) high-resolution scans for Si 2p electrons of MMT and WS_2/MMT, scans for (**c**) W 4f and (**d**) S 2p electrons of WS_2/MMT.

MMT, the intensity of the reflections of WS_2 is relatively lower in the pattern of WS_2/MMT-0.5, indicating the lower content of WS_2. The reflection assigned to (100) plane of WS_2 has higher intensity in the WS_2/MMT-2, while the diffraction peak corresponding to (002) plane is broader and lower, which could be attributed to lower stacking of WS_2 layers.

The interface interaction was studied by FTIR analysis. In the FTIR spectrum of MMT (Fig. 2b), the bands due to vibration of Si–O is found at 471 and 1022 cm^{-1}, indicating that a silicon-oxygen tetrahedron exists in the layered structure of MMT. The broad band at 3620 cm^{-1} is due to the aluminum hydroxy stretching vibration. The hydroxy bending vibration and H–O–H stretching vibration corresponding to hydrogen bonding water could be observed at 1637 and 3453 cm^{-1}. The bands at 1401, 1613 and 3125 cm^{-1} in the FTIR spectrum of WS_2 are associated with the W–S bending vibration and stretching vibration[41]. For WS_2/MMT, the bands corresponding to hydroxy decrease significantly, and the band of Si–O shifts to 1037 cm^{-1} from 1022 cm^{-1}, which suggests the interface interaction between WS_2 and MMT.

The chemical statuses of the samples were investigated using XPS. Fig. 3a shows the XPS survey spectra of samples in the range 0–700 eV. Compared with the XPS spectrum survey of MMT, the peaks of W and S are observed in the WS_2/MMT. The binding energy of Si 2p in WS_2/MMT (Fig. 3b) shifts to a little higher energy state compared with that of MMT, indicating electronic interaction between WS_2 and MMT. The W 4 f peaks of WS_2/MMT (Fig. 3c) are located at the binding energies of 32.2, 34.3, 36.1 and 38.2 eV, respectively. The binding energies of W $4f_{7/2}$ and W $4f_{5/2}$ peaks at 32.2 and 34.3 eV are correspond to W^{4+}, and the binding energies at 36.1 and 38.2 eV are attributed to W^{6+} (oxide states), which might be due to the partial oxidation of tungsten on the surface and the interface interaction between WS_2 and MMT. In the scans of S 2p electrons of WS_2/MMT (Fig. 3d), the binding energies of S $2p_{3/2}$ and S $2p_{1/2}$ peaks are 161.9 and 163.3 eV, respectively.

The morphologies of samples were characterized with SEM. In the SEM image of MMT (Fig. 4a), the sample presents a lamellar morphology and smooth surface, which is favorable for the supporting of WS_2. The WS_2 synthesized by hydrothermal method exhibits the agglomerated particles with irregular shapes (Fig. 4c). For WS_2/MMT (Fig. 4e), WS_2 and MMT exhibit two dimensional morphology and stack with each other to form layer structure. In the WS_2/MMT composites, MMT could reduce the agglomeration of WS_2. The energy disperse spectrum of WS_2/MMT indicates that the mass contents of W and S element are 29.84 Wt% and 10.60 Wt%, which is in accord with the theoretical element ratio of WS_2.

Further details of the microstructure could be obtained by TEM and HRTEM. The TEM image of MMT (Fig. 4b) shows dispersed nanosheet. As shown in Fig. 4d, the synthesized WS_2 is irregular nanoparticle. The HRTEM image indicates that the (002) plane WS_2 nanoparticle is 0.62 nm, in accordance with XRD result. From the TEM and HRTEM of WS_2/MMT (Fig. 4f), the microstructure of sample exhibits composite nanosheets, and

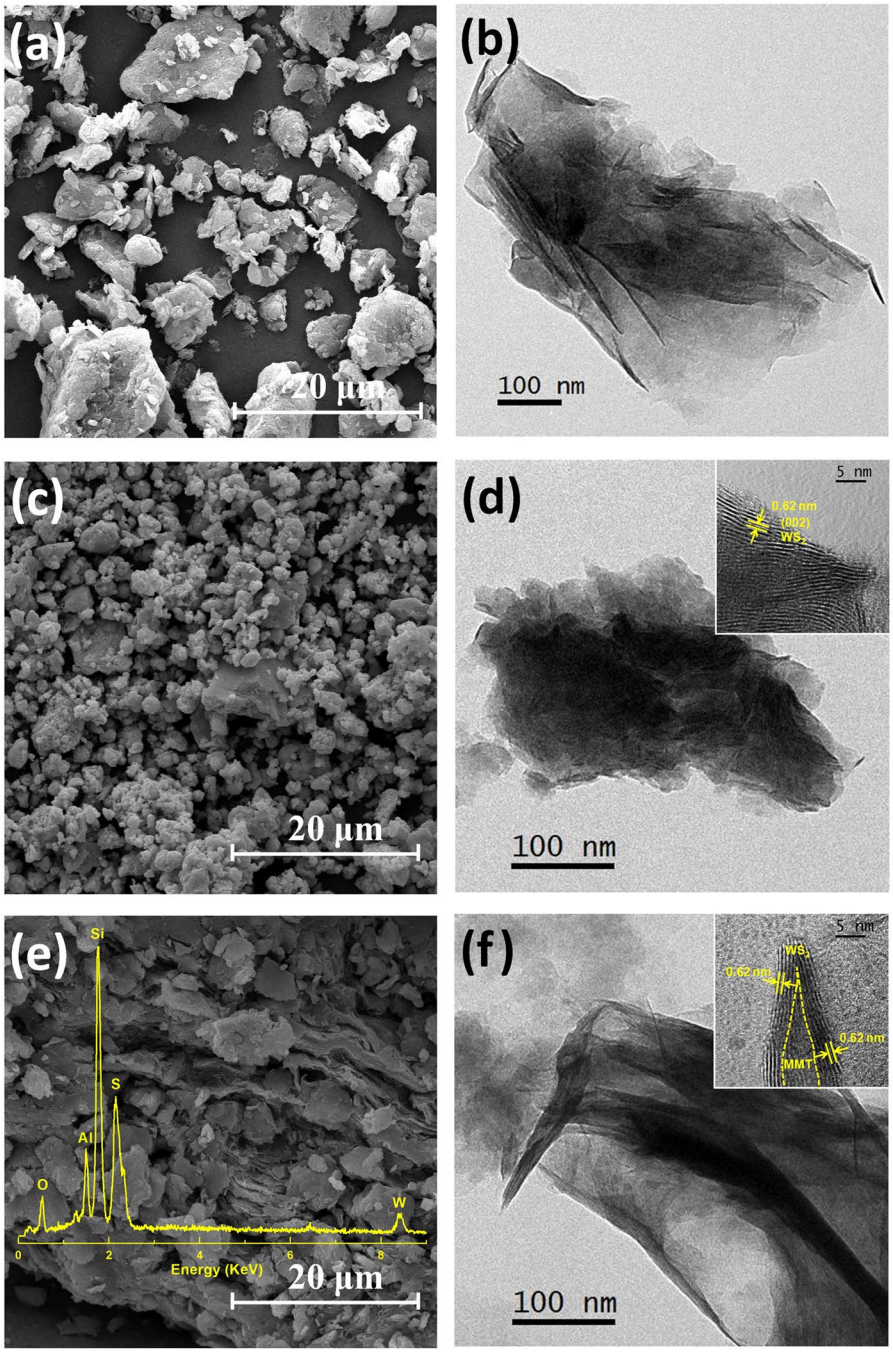

Figure 4. Morphologies of the samples. SEM images of (**a**) MMT, (**c**) WS_2 and (**e**) WS_2/MMT and the EDS spectrum. TEM images of (**b**) MMT, (**d**) WS_2 and (**f**) WS_2/MMT and the HRTEM image.

WS_2 nanosheets are assembled parallelly on MMT. The WS_2 nanosheets could possess better dispersibility and expose more catalytic reaction edges attributed to support of MMT.

The specific surface area was characterized by nitrogen adsorption-desorption isotherms. In the curves of MMT and WS_2/MMT (Fig. 5a), the type IV adsorption branches are corresponding to the mesoporous structure. The specific surface area of WS_2/MMT and MMT are calculated to be 16.13 and 38.02 $m^2 \cdot g^{-1}$, respectively. No hysteresis loop is observed in the curve of WS_2, and the specific surface area is 6.56 $m^2 \cdot g^{-1}$. Compared with WS_2, WS_2/MMT has relatively higher specific surface area, and it might be because MMT could reduce the stack and inhibit the agglomeration of WS_2 nanosheets. The pore size distributions are shown in Fig. 5b. The average pore size of MMT is about 3 nm, while those of WS_2 and WS_2/MMT are around 40 nm. Due to the support of MMT, WS_2/MMT composite nanosheets possess larger special surface area than WS_2, which might provide more reactive sites to enhance photocatalytic activity.

The UV–vis diffuse reflectance spectra of samples are shown in Fig. 6a. The visible light absorption of MMT is very weak. WS_2 and WS_2/MMT exhibit considerable visible absorption, which is consistent with the black color of

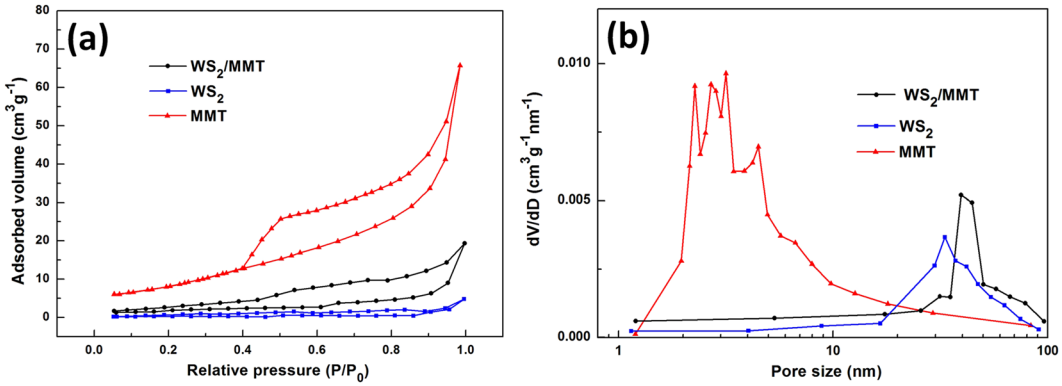

Figure 5. Specific surface area of the samples. (**a**) N_2 adsorption/desorption isotherm curves and (**b**) pore-size distributions of MMT, WS_2 and WS_2/MMT.

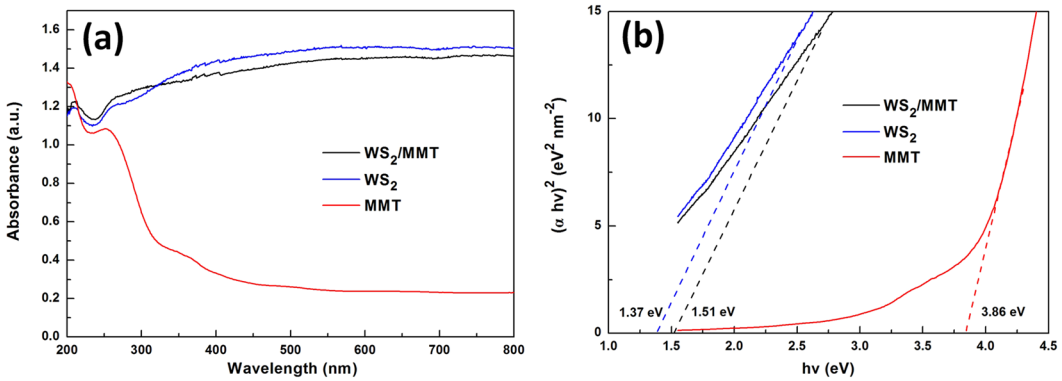

Figure 6. Energy band structure of MMT, WS_2 and WS_2/MMT. (**a**) UV-vis diffuse reflectance spectra, (**b**) the corresponding plots of $(\alpha hv)^2$ vs. photon energy (hv).

the samples. It is of great significance for visible light photocatalytic application[42]. The band gap energies of MMT, WS_2 and WS_2/MMT (Fig. 6b) are 3.86, 1.37 and 1.51 eV, respectively. Compared with WS_2, WS_2/MMT possesses larger band gap energy, which could be due to the effects of the few layered WS_2 and MMT.

Compared with the PL peak of WS_2 (Fig. S1), the peak shape and position of WS_2/MMT are similar, while the peak intensity is higher. It might be related to luminescence-inactive multilayer structure in WS_2. In the PL spectrum of MMT, the peak at 354 and 398 nm could be due to the intrinsic defects of surplus oxygen on the surface and intrinsic diamagnetic defect center, respectively. The PL peak intensity of WS_2/MMT is weaker than that of MMT, which is attributed to the less recombination of photo-generated carriers.

Photodegradation of organic dyes was applied to evaluate the photocatalytic abilities of samples for aqueous phase reactions. The variation of decoloration rate with MMT, WS_2, WS_2/MMT, WS_2/MMT-0.5 and WS_2/MMT-2 as catalysts is shown in Fig. 7a. The RhB aqueous solution is stable with visible light irradiation during 1 h, and the decoloration rate has hardly the change without catalyst. Adsorption equilibrium was reached without light irradiation for 15 min, and physical adsorption of samples was recorded. MMT has the highest adsorption capacity up to 17.0%, and the adsorption rate of WS_2 is lowest. The WS_2/MMT has higher adsorption rate than WS_2, and the adsorption rate has an increase tendency with the increasing of MMT content. It might be because the special structure of MMT, and the high specific surface area and abundant surface hydroxyl groups are in favor of the adsorption for RhB[43,44]. WS_2/MMT has the highest degradation speed, and the overall decoloration rate of RhB is up to 99.8% after visible light irradiation for 45 min. The degradation speeds of WS_2/MMT-0.5 and WS_2/MMT-2 are higher than that of WS_2, but lower than WS_2/MMT. Photocatalytic ability of WS_2/MMT composite nanosheets is enhanced via the support of MMT. It might be because the MMT sheets prevent WS_2 nanosheets aggregation, and improve the hydrophilicity and dispersibility of aqueous phase, which could supply composites more reactive sites. As shown in Fig. S4, the photocatalytic ability of WS_2/MMT does not show obvious change after four cycles, indicating the high stability of WS_2/MMT in the aqueous phase photocatalytic reaction process. WS_2/MMT also shows excellent photodegradation performance for Methylene blue (MB), Methyl orange (MO) and Congo red (CR) in the aqueous phase (Fig. S5). The photodegradation of RhB was observed to follow pseudo-first-order kinetics[21] according to the formula ($\ln(C/C_0 = -kt)$), where C and C_0 is the homologous and initial concentration, and k is apparent reaction rate constant. The apparent reaction rate constants of WS_2/MMT and WS_2 are 0.16 and 0.09 min^{-1} (Fig. S6), indicating the higher photocatalytic ability of WS_2/MMT.

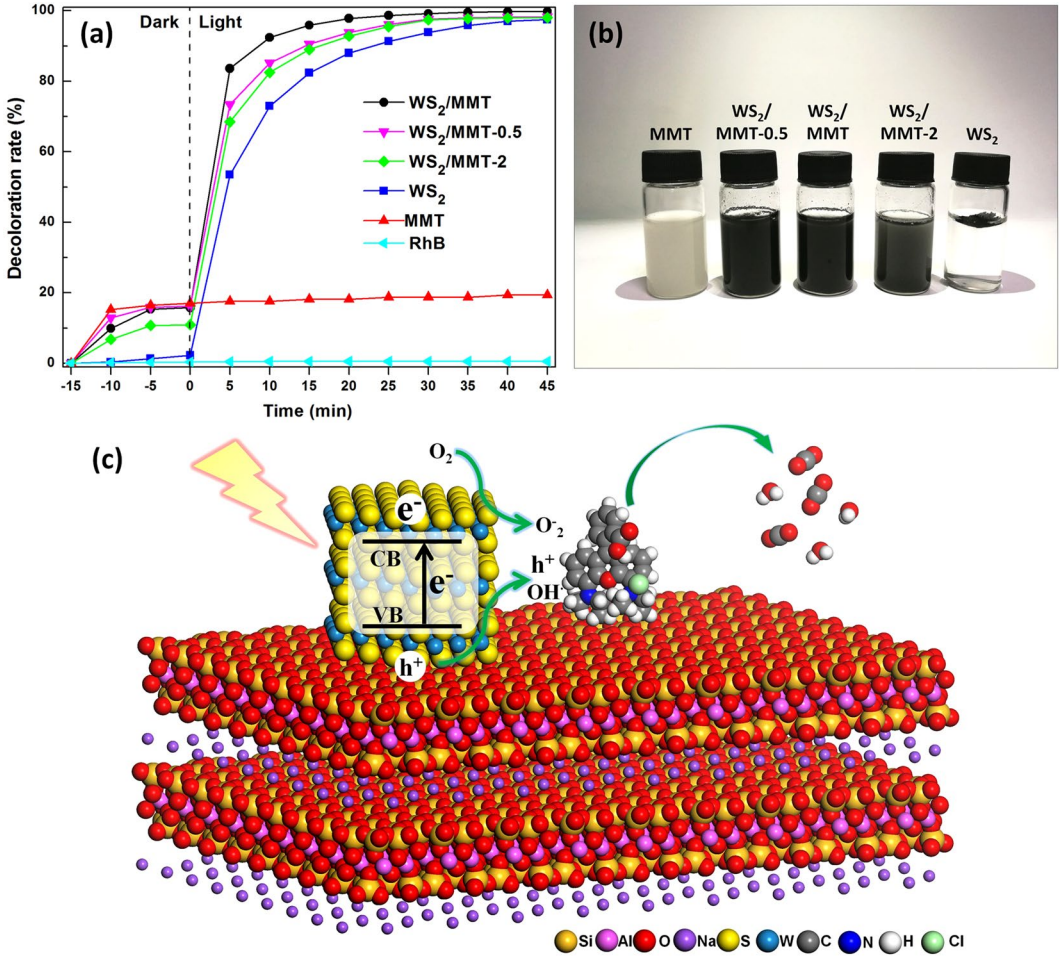

Figure 7. Photocatalytic activity and possible reaction mechanism. (**a**) Decoloration of RhB with MMT, WS_2, WS_2/MMT, WS_2/MMT-0.5 and WS_2/MMT-2 as catalysts. (**b**) Digital photograph of the samples in aqueous phase. (**c**) Schematic illustration for possible photocatalytic reaction mechanism.

In Fig. 7b, WS_2/MMT composite nanosheets uniformly disperse in water, while WS_2 almost floated on the aqueous phase, which could be attributed to the hydrophobicity of hydrothermally synthesized WS_2. Contact angles of MMT, WS_2/MMT and WS_2 (Fig. S2) are 18.7°, 32.3° and 54.5°, respectively. With the supporting of MMT, WS_2/MMT has better hydrophilicity than WS_2.

Discussion

As shown in Fig. S3, the UV–vis absorption peak of RhB is located at 554 nm, while no obvious absorption peak is observed after RhB is photodegraded. The possible photocatalysis mechanism for the degradation of RhB is shown in Fig. 7c. With the excitation of visible light, the photoinduced electrons (e^-) and holes (h^+) are generated in WS_2, respectively[45]. hydroxyl groups could capture h^+ to form hydroxyl radicals ($OH^·$), which could restrain recombination and improve the photocatalytic ability[46]. The photoexcited e^- electrons might induce the O_2^- with O_2, and these h^+, $OH^·$ and O_2^- could photo-oxidize organic molecules RhB.

In conclusion, WS_2/MMT nanosheets were prepared by the hydrothermal method, which were utilized as an efficient hydrophilic photocatalyst for aqueous phase reactions. Few-layered WS_2 nanosheets are grown parallelly on MMT, and MMT could reduce the stack and inhibit the agglomeration of WS_2 nanosheets, which supply composites more catalytic reaction sites. With WS_2/MMT as photocatalyst, the overall decoloration capacity of RhB was up to 99.8%. Through the support of MMT, WS_2/MMT possesses high hydrophilicity and dispersibility of aqueous phase, which is conducive to the enhancement of catalytic ability. The WS_2/MMT composite nanosheets have potential to treat organic waste water. The strategy could provide insights for construction of efficient hydrophilic photocatalyst with excellent activity for environmental treatment.

Methods

Materials. The montmorillonite (MMT) used was obtained from Zhejiang Sanding Technology Co. Ltd. (Zhejiang, China). It consisted primarily of MMT (>97%) with minor impurity of quartz. The chemical compositions of MMT were as follows: SiO_2 61.5 Wt%, Al_2O_3 19.3 Wt%, MgO 3.5 Wt%, Fe_2O_3 1.4 Wt%, Na_2O 2.8 Wt%, CaO 2.5 Wt%, K_2O 0.6 Wt%, and the loss on ignition was approximately 8.4 Wt%. Tungsten chloride (WCl_6),

thioacetamide (CH_3CSNH_2) and Rhodamine B were purchased from Sinopharm Chemical Reagent Co. Ltd. All reagents were analytical grade and used without further purification[46].

Preparation. The WS_2/montmorillonite (WS_2/MMT) composite nanosheets were synthesized by a facile hydrothermal method. In a typical experiment, 1.785 g of tungsten chloride and 3.415 g of thioacetamide were dissolved in 60 mL of deionized water and mechanically stirred for 30 min at room temperature. 1.000 g of MMT was added in the solution, and the mixture suspension was stirred for another 30 min and sonicated for 10 min at room temperature. Then, the suspension was transferred into a 100 mL Teflon-lined stainless steel autoclave, heated up to 220 °C, and kept for 24 h[11]. After cooling naturally, the precipitates were collected by centrifugation, and subsequently washed several times with deionized water. The final products were obtained after drying at 60 °C for 24 h. For comparison, pure WS_2 samples were synthesized by a similar process, without MMT. Other samples were similarly prepared with different additive amounts of tungsten chloride and thioacetamide. A sample prepared with 0.893 g of tungsten chloride and 1.708 g of thioacetamide was labeled as WS_2/MMT-0.5. A sample with 3.570 g of tungsten chloride and 6.830 g of thioacetamide was labeled as WS_2/MMT-2[6].

Characterization. Powder X-ray diffraction (XRD) patterns of the samples were obtained on a RIGAKU D/max-2550 PC X-ray diffractometer with Cu Kα radiation ($\lambda = 0.15406$ nm) at a scan rate of 0.02°/s[32]. Fourier transform infrared (FTIR) spectra of the samples were obtained between 4000 and 400 cm^{-1} on a Nicolet Nexus 670 FTIR spectrophotometer using KBr pellets. Scanning electron microscopy (SEM) images were obtained with a JEOL JSM-6360LV scanning electron microscope at an accelerating voltage of 5 kV, which equipped with energy dispersive spectrometer (EDS). Transmission electron microscopy (TEM) and high-resolution TEM (HRTEM) were operated with a JEOL JEM-2100F transmission electron microscope at an acceleration voltage of 200 kV[42]. The N_2 adsorption-desorption isotherms were record at 77 K and analyzed using an ASAP 2020 surface area analyzer. X-ray photoelectron spectroscopy (XPS) measurements were performed using an ESCALAB 250 spectrometer. The UV-vis diffuse reflectance spectra (UV-vis DRS) were obtained with a Shimadzu UV2450 UV-vis spectrophotometer, and barium sulfate was used as reference. The photoluminescence (PL) experiment were conducted on a Hitachi F-4500 fluorescence spectrometer using an excitation wavelength of 254 nm[3]. The contact angles of the samples were measured using the sessile-drop technique using a goniometer (GBX, France).

Photocatalytic activity evaluation. Photodegradation of Rhodamine B (RhB) was selected as a typical reaction to evaluate the photocatalytic activity of samples for aqueous phase reactions. The light source was a 150 W high pressure mercury lamp with wave length $\lambda > 400$ nm. In a typical photocatalytic experiment, 100 mg of catalyst was added in 100 mL RhB aqueous solution (0.02 mmol/L). Firstly, the mixture suspension was magnetically stirred in the dark for 15 min to ensure the establishment of an adsorption-desorption equilibrium between the catalyst and RhB aqueous solution. Then, the reaction vessel was positioned with light irradiation, and 1 mL of 3% H_2O_2 was added as oxidant to initiate the reaction. About 3 mL of analytical sample was withdrawn from the reaction suspension every 5 min, and the catalyst was removed by a centrifuge. The concentration of the photodegradable compound was monitored by recording the absorbance (A) of the clarified solution at 554 nm with an UV-visible spectrophotometer. The decoloration rate (%) was calculated from the formula: decoloration rate (%) $= (A_0 - A)/A_0 \times 100\%$, where A_0 was the initial absorbance, and A was the absorbance at homologous times[25]. The catalyst was centrifuged for the next cycle. Photocatalytic degradation of Methylene blue (MB), Methyl orange (MO) and Congo red (CR) were performed under the similar condition.

Data availability

The data that support the findings of this study are available from the corresponding author on reasonable request.

Received: 4 January 2019; Accepted: 15 August 2019;
Published online: 08 November 2019

References

1. Woods, J. M. *et al.* One-step synthesis of MoS_2/WS_2 layered heterostructures and catalytic activity of defective transition metal dichalcogenide films. *ACS Nano* **10**, 2004–2009 (2016).
2. Fu, Q. *et al.* Synthesis and enhanced electrochemical catalytic performance of monolayer $WS_{2(1-x)}Se_{2x}$ with a tunable band gap. *Adv. Mater.* **27**, 4732–4738 (2015).
3. Zhong, Y. *et al.* Band-gap-matched CdSe QD/WS_2 nanosheet composite: Size-controlled photocatalyst for high-efficiency water splitting. *Nano Energy* **31**, 84–89 (2017).
4. Cao, Y. *et al.* Defect-induced efficient dry reforming of methane over two-dimensional Ni/h-boron nitride nanosheet catalysts. *Appl. Catal. B-Environ.* **238**, 51–60 (2018).
5. Han, X., Yu, Y., Huang, Y., Liu, D. & Zhang, B. Photogenerated carriers boost water splitting activity over transition-metal/semiconducting metal oxide bifunctional electrocatalysts. *ACS Catal.* **7**, 6464–6470 (2017).
6. Peng, K., Fu, L., Yang, H., Ouyang, J. & Tang, A. Hierarchical MoS2 intercalated clay hybrid nanosheets with enhanced catalytic activity. *Nano Res.* **10**, 570–583 (2016).
7. Li, N. *et al.* Stable multiphasic 1T/2H $MoSe_2$ nanosheets integrated with 1D sulfide semiconductor for drastically enhanced visible-light photocatalytic hydrogen evolution. *Appl. Catal. B-Environ.* **238**, 27–37 (2018).
8. Zhao, Y. *et al.* Defect-rich ultrathin ZnAl-layered double hydroxide nanosheets for efficient photoreduction of CO_2 to CO with water. *Adv. Mater.* **27**, 7824–7831 (2015).
9. Pumera, M. & Sofer, Z. Towards stoichiometric analogues of graphene: graphane, fluorographene, graphol, graphene acid and others. *Chem. Soc. Rev.* **46**, 4450–4463 (2017).
10. Liu, H., Chen, D., Wang, Z., Jing, H. & Zhang, R. Microwave-assisted molten-salt rapid synthesis of isotype triazine-/heptazine based g-C_3N_4 heterojunctions with highly enhanced photocatalytic hydrogen evolution performance. *Appl. Catal. B-Environ.* **203**, 300–313 (2017).
11. Peng, K., Fu, L., Ouyang, J. & Yang, H. Emerging parallel dual 2D composites: natural clay mineral hybridizing MoS_2 and interfacial structure. *Adv. Funct. Mater.* **26**, 2666–2675 (2016).

12. Shi, J. *et al*. Temperature-mediated selective growth of MoS_2/WS_2 and WS_2/MoS_2 vertical stacks on au foils for direct photocatalytic applications. *Adv. Mater.* **28**, 10664–10672 (2016).
13. Sang, Y. *et al*. From UV to near-infrared, WS_2 nanosheet: A novel photocatalyst for full solar light spectrum photodegradation. *Adv. Mater.* **27**, 363–369 (2015).
14. Su, D., Dou, S. & Wang, G. WS_2@graphene nanocomposites as anode materials for Na-ion batteries with enhanced electrochemical performances. *Chem. Commun.* **50**, 4192 (2014).
15. Zhong, Y., Zhao, G., Ma, F., Wu, Y. & Hao, X. Utilizing photocorrosion-recrystallization to prepare a highly stable and efficient CdS/WS_2 nanocomposite photocatalyst for hydrogen evolution. *Appl. Catal. B-Environ.* **199**, 466–472 (2016).
16. Raza, F. *et al*. Structuring Pd nanoparticles on 2H-WS_2 nanosheets induces excellent photocatalytic activity for cross-coupling reactions under visible light. *J. Am. Chem. Soc.* **139**, 14767–14774 (2017).
17. Zhao, X., Ma, X., Sun, J., Li, D. & Yang, X. Enhanced catalytic activities of surfactant-assisted exfoliated WS_2 nanodots for hydrogen evolution. *ACS Nano* **10**, 2159–2166 (2016).
18. Zou, J.-P. *et al*. Fabrication of novel heterostructured few layered WS_2-Bi_2WO_6/$Bi_{3.84}W_{0.16}O_{6.24}$ composites with enhanced photocatalytic performance. *Appl. Catal. B-Environ.* **179**, 220–228 (2015).
19. Wen, Y., Zhang, H. & Zhang, S. One-step gas–solid reaction synthesis of W@WS_2 nanorattles and their novel catalytic activity. *Nanoscale* **6**, 13090–13096 (2014).
20. Vattikuti, S. V. P., Byon, C. & Reddy, C. V. Preparation and improved photocatalytic activity of mesoporous WS_2 using combined hydrothermal-evaporation induced self-assembly method. *Mater. Res. Bull.* **75**, 193–203 (2016).
21. Koyyada, G. *et al*. Enhanced solar light-driven photocatalytic degradation of pollutants and hydrogen evolution over exfoliated hexagonal WS_2 platelets. *Mater. Res. Bull.* **109**, 246–254 (2019).
22. Ma, X. *et al*. Evidence of direct Z-scheme g-C_3N4/WS_2 nanocomposite under interfacial coupling: First-principles study. *J. Alloy. Comp.* **788**, 1–9 (2019).
23. Yang, J. *et al*. Two-dimensional hybrid nanosheets of tungsten disulfide and reduced graphene oxide as catalysts for enhanced hydrogen evolution. *Angew. Chem.-Int. Edit.* **52**, 13751–13754 (2013).
24. Peng, K. *et al*. One-step hydrothermal growth of MoS_2 nanosheets/CdS nanoparticles heterostructures on montmorillonite for enhanced visible light photocatalytic activity. *Appl. Clay Sci.* **175**, 86–93 (2019).
25. Peng, K., Fu, L., Yang, H. & Ouyang, J. Perovskite $LaFeO_3$/montmorillonite nanocomposites: synthesis, interface characteristics and enhanced photocatalytic activity. *Sci. Rep.* **6**, 19723 (2016).
26. Li, X. & Tang, A. Pd modified kaolinite nanocomposite as a hydrogenation catalyst. *RSC Adv.* **6**, 15585–15591 (2016).
27. Yan, Z., Yang, H., Ouyang, J. & Tang, A. *In situ* loading of highly-dispersed CuO nanoparticles on hydroxyl-group-rich SiO_2-AlOOH composite nanosheets for CO catalytic oxidation. *Chem. Eng. J.* **316**, 1035–1046 (2017).
28. Li, X., Ouyang, J., Zhou, Y. & Yang, H. Assembling strategy to synthesize palladium modified kaolin nanocomposites with different morphologies. *Sci. Rep.* **5**, 13763 (2015).
29. Yan, Z., Fu, L., Yang, H. & Ouyang, J. Amino-functionalized hierarchical porous SiO_2-AlOOH composite nanosheets with enhanced adsorption performance. *J. Hazard. Mater.* **344**, 1090–1100 (2018).
30. Peng, K., Fu, L., Li, X., Ouyang, J. & Yang, H. Stearic acid modified montmorillonite as emerging microcapsules for thermal energy storage. *Appl. Clay Sci.* **138**, 100–106 (2017).
31. Peng, K., Zhang, J., Yang, H. & Ouyang, J. Acid-hybridized expanded perlite as a composite phase-change material in wallboards. *RSC Adv.* **5**, 66134–66140 (2015).
32. Li, X., QianYang, Ouyang, J., Yang, H. & Chang, S. Chitosan modified halloysite nanotubes as emerging porous microspheres for drug carrier. *Appl. Clay Sci.* **126**, 306–312 (2016).
33. Peng, K., Yang, H. & Ouyang, J. Tungsten tailing powders activated for use as cementitious material. *Powder Technol.* **286**, 678–683 (2015).
34. Peng, K., Lv, C. & Yang, H. Novel preparation of glass ceramics from amorphized tungsten tailings. *Ceram. Int.* **40**, 10291–10296 (2014).
35. Gao, S. *et al*. Triboelectric nanogenerator powered electrochemical degradation of organic pollutant using Pt-free carbon materials. *ACS Nano* **11**, 3965–3972 (2017).
36. Li, X. *et al*. Facile synthesis of wormhole-like mesoporous tin oxide via evaporation-induced self-assembly and the enhanced gas-sensing properties. *Nanoscale Res. Lett.* **13**, 14 (2018).
37. Liu, W. *et al*. Kinetic and mechanism studies on pyrolysis of printed circuit boards in the absence and presence of copper. *ACS Sustainable Chem. & Eng.* **7**, 1879–1889 (2018).
38. Li, X. & Peng, K. Synthesis of 3D mesoporous alumina from natural clays for confining CdS nanoparticles and enhanced photocatalytic performances. *Appl. Clay Sci.* **165**, 188–196 (2018).
39. Sun, M., Zhao, Q., Du, C. & Liu, Z. Enhanced visible light photocatalytic activity in BiOCl/SnO_2: heterojunction of two wide band-gap semiconductors. *RSC Adv.* **5**, 22740–22752 (2015).
40. Liu, X., Su, Y., Zhao, Q., Du, C. & Liu, Z. Constructing $Bi_{24}O_{31}Cl_{10}$/BiOCl heterojunction via a simple thermal annealing route for achieving enhanced photocatalytic activity and selectivity. *Sci. Rep.* **6**, 28689 (2016).
41. Wu, J. *et al*. Glucose aided preparation of tungsten sulfide/multi-wall carbon nanotube hybrid and use as counter electrode in dye-sensitized solar cells. *ACS Appl. Mater. Interfaces* **4**, 6530–6536 (2012).
42. Li, X. & Peng, K. Hydrothermal synthesis of MoS_2 nanosheet/palygorskite nanofiber hybrid nanostructures for enhanced catalytic activity. *Appl. Clay Sci.* **162**, 175–181 (2018).
43. Peng, K. & Yang, H. Carbon hybridized montmorillonite nanosheets: preparation, structural evolution and enhanced adsorption performance. *Chem. Commun.* **53**, 6085–6088 (2017).
44. Yan, Z., Fu, L., Zuo, X. & Yang, H. Green assembly of stable and uniform silver nanoparticles on 2D silica nanosheets for catalytic reduction of 4-nitrophenol. *Appl. Catal. B-Environ.* **226**, 23–30 (2018).
45. Li, X., Peng, K., Chen, H. & Wang, Z. TiO_2 nanoparticles assembled on kaolinites with different morphologies for efficient photocatalytic performance. *Sci. Rep.* **8**, 11663 (2018).
46. Li, X. & Peng, K. $MoSe_2$/montmorillonite composite nanosheets: hydrothermal synthesis, structural characteristics, and enhanced photocatalytic activity. *Minerals* **8**, 268 (2018).

Acknowledgements

This work was supported by National Natural Science Foundation of China (51804242, 51772237, 51704030), the China Postdoctoral Science Foundation (2018T111054, 2017M623182, 2017M610617) and Natural Science Basic Research Plan in Shaanxi province of China (2018JQ5155). Shaanxi Science & Technology co-ordination & Innovation project (No. 2015KTCL01-13) Shaanxi Innovation Capacity Support Program (2018TD-031).

Author contributions

K.P. and H.W. conceived the experiment. K.P., X.L. and J.W. performed the experiments. Z.C., L.S. and X.F. were involved in scientific discussion and data analysis. K.P. wrote initial drafts of the work. All authors commented on the manuscript.

Competing interests

The authors declare no competing interests.

Additional information

Supplementary information is available for this paper at https://doi.org/10.1038/s41598-019-52191-9.

Correspondence and requests for materials should be addressed to H.W.

Reprints and permissions information is available at www.nature.com/reprints.

Publisher's note Springer Nature remains neutral with regard to jurisdictional claims in published maps and institutional affiliations.